Stripe order on the spin-1 stacked honeycomb lattice in $Ba_2Ni(PO_4)_2$

Arvind Yogi,[1,*] A. K. Bera,[2,†] Arvind Maurya,[1] Ruta Kulkarni,[1] S. M. Yusuf,[2] A. Hoser,[3] A. A. Tsirlin,[4,‡] and A. Thamizhavel[1,§]

[1]*Department of Condensed Matter Physics and Materials Science, Tata Institute of Fundamental Research, Homi Bhabha Road, Colaba, Mumbai 400 005, India*

[2]*Solid State Physics Division, Bhabha Atomic Research Centre, Mumbai 400085, India*

[3]*Helmholtz-Zentrum Berlin für Materialien und Energie, 14109 Berlin, Germany*

[4]*Experimental Physics VI, Center for Electronic Correlations and Magnetism, Institute of Physics, University of Augsburg, 86135 Augsburg, Germany*

(Received 22 August 2016; published 3 January 2017)

We report a comprehensive investigation of the crystal structure and magnetic behavior of the $S = 1$ compound $Ba_2Ni(PO_4)_2$ with a honeycomblike topology of the spin lattice. Magnetic susceptibility and specific-heat data reveal two successive transitions at $T_{N1} = 5$ K and $T_{N2} = 4.6$ K. Additionally, these data demonstrate a broad peak at $T_{max} \sim 8$ K, indicative of the short-range magnetic order above T_{N1}, whereas below T_{N1} field-induced transitions around 4 and 10 T are identified from the magnetization measurements. Neutron diffraction in zero field establishes stripe antiferromagnetic order below T_{N2} with the ordered moment of $1.75(8)\mu_B/Ni^{2+}$ at 1.5 K. Density-functional band-structure calculations reveal the leading interaction $J_3 = 3.5$ K running perpendicular to the honeycomb planes, and weaker interactions $J_1 = 0.5$ K and $J_4 = 1.8$ K within the honeycomb planes, whereas the stripe order is stabilized by the diagonal interlayer interaction $J_2 = 1.3$ K that frustrates J_1. This is in contrast to the usually expected scenario where the competing second- and third-neighbor interactions on the honeycomb lattice stabilize the stripe order. The Ni^{2+} ions feature a sizable easy-plane anisotropy $A \simeq 10.5$ K, but the position of the easy plane changes from one atom to another, thus amplifying magnetic frustration.

DOI: 10.1103/PhysRevB.95.024401

I. INTRODUCTION

Two-dimensional honeycomb lattice is one of the most interesting low-dimensional geometries of magnetic systems. Its low bond connectivity gives rise to strong quantum effects. For a spin-$\frac{1}{2}$ antiferromagnet on the honeycomb lattice with only nearest-neighbor interactions within the plane, the nearly twofold reduction in the ordered moment is expected due to quantum fluctuations, from $1.0\mu_B$ in the classical case to $0.55\mu_B$ in the quantum regime [1,2]. Magnetic order on the honeycomb lattice can be suppressed completely via frustration by second- and third-neighbor interactions [3–7] or via a combination of anisotropic exchange interactions in the spirit of the Kitaev model [8], where a spin-liquid state is stabilized for a wide range of parameters.

Several honeycomb-lattice antiferromagnets, including $Na_2Cu_2TeO_6$ [9], $Na_3Cu_2SbO_6$ [10], and Cu_5SbO_6 [11], indeed lack long-range magnetic order and reveal a spin-singlet ground state. However, this ground state is rooted in the dimerization arising from geometrical distortions of the honeycomb planes [12–14]. In Ni^{2+}-based honeycomb systems, zigzag order prevails [15–19]. It features zigzag chains of parallel spins and, alternatively, can be described as a state where each spin is surrounded by two spins having the same direction and one spin having the opposite direction. Other types of collinear magnetic order have been observed too [20,21]. In the Néel state, each spin is surrounded by three spins having the opposite direction (i.e., all nearest-neighbor spins are antiparallel), whereas in the stripe state each spin is surrounded by two antiparallel and one parallel spins. The type of magnetic order is usually controlled by second- and third-neighbor couplings on the honeycomb lattice [15,20].

Here, we report the magnetic ground state and magnetic properties of the spin-1 antiferromagnet $Ba_2Ni(PO_4)_2$ with a honeycomblike spin lattice. This compound belongs to the phosphate family $A_2M(PO_4)_2$ (A = Ba and Sr; M = Cu, Ni, Co, Mn) having monoclinic crystal structures [22–24]. $Ba_2Ni(PO_4)_2$ was first prepared by Elbali *et al.* [22], who presented its basic properties only. Here, we present a comprehensive study of this compound. We demonstrate that in zero field it undergoes two consecutive magnetic transitions and at low temperatures forms stripe antiferromagnetic (AFM) order, which is rarely seen in honeycomb systems. The origin of this state is rationalized microscopically using the model of a stacked honeycomb lattice with frustrating interactions between the honeycomb planes. Additionally, we observe a sequence of field-induced transitions and a competition of single-ion anisotropies that amplifies magnetic frustration in $Ba_2Ni(PO_4)_2$.

II. METHODS

Polycrystalline samples of $Ba_2Ni(PO_4)_2$ were synthesized by a conventional solid-state reaction route using Ba_2CO_3 (99.999%, Alfa Aesar), NiO (99.999%, Aldich), and $NH_4H_2PO_4$ (99.999%, Alfa Aesar) as starting materials. The starting materials were mixed in acetone medium and ground in an agate mortar, put into a high pure alumina (99.999%) crucible, and heated at 450 °C for 6 h and at 650 °C for 24 h in air in order to release H_2O, NH_3, and CO_2. The resulting

*arvind.yogi@tifr.res.in
†akbera@barc.gov.in
‡altsirlin@gmail.com
§thamizh@tifr.res.in

powder was then ground and heated at 1000 °C for 48 h with several intermediate grindings and pelletizations. After each heating, the sample was cooled down at the rate of 120 °C/h to room temperature and reground to improve homogeneity. The synthesized sample was light yellow in color. The progress of the reaction was followed by powder x-ray diffraction (XRD), and the final reaction rendered the phase-pure powder sample.

Magnetic susceptibility $\chi(T)$ measurements were performed using the SQUID magnetometer from Quantum Design. Isothermal magnetization and heat-capacity $C_p(T)$ measurements were done using a commercial Physical Property Measurement System (PPMS, Quantum Design).

Powder neutron diffraction patterns were recorded by using the cold-neutron focusing diffractometer E6 ($\lambda = 2.45$ Å) at HZB, Germany. The powdered sample was loaded into a cylindrical vanadium container. Low-temperature measurements were performed in a standard Orange cryostat. The diffraction data were analyzed by the Rietveld method using the program FULLPROF [25].

Scalar-relativistic and full-relativistic density-functional (DFT) band-structure calculations were performed in the FPLO code [26] using local density approximation (LDA) for the exchange-correlation potential [27]. Reciprocal space was sampled by a k mesh with 104 and 32 k points in the symmetry-irreducible part of the first Brillouin zone for the crystallographic unit cell and for the supercell doubled along the a direction, respectively. Strong correlation effects in the Ni $3d$ shell were taken into account on the mean-field LSDA+U level with the onsite Coulomb repulsion $U_d = 6$ eV, Hund's coupling $J_d = 1$ eV, and fully-localized-limit double-counting correction [28,29].

Parameters of the spin Hamiltonian

$$\hat{H} = \sum_{\langle ij \rangle} J_{ij} \mathbf{S}_i \mathbf{S}_j - \sum_i A\, S^2_{i\varkappa_i} \qquad (1)$$

were derived from DFT calculations, as further explained in Sec. III F. Here, the summation is over bonds $\langle ij \rangle$, J_{ij} are isotropic exchange couplings, A stands for the single-ion anisotropy, $\varkappa_i$ denotes the direction of the easy ($A > 0$) or hard ($A < 0$) axis for site i, and $S_{i\varkappa_i}$ is the component of the local spin $\mathbf{S}_i$ along this direction. Additionally, orbital energies and hopping parameters were extracted from tight-binding fits of the LDA band structure using Wannier functions implemented in FPLO.

III. RESULTS

A. X-ray diffraction and crystal structure

The crystal structure of $Ba_2Ni(PO_4)_2$ has been investigated by the room-temperature powder x-ray diffraction measurement (Fig. 1). Rietveld analysis confirms that the compound crystallizes in the monoclinic space group $P2_1/n$ (space group No. 14). It also confirms the single-phase nature of the powder sample. The values of the lattice parameters are found to be $a = 5.32102(9)$ Å, $b = 8.80268(16)$ Å, and $c = 16.0958(3)$ Å, and $\beta = 90.704(9)^\circ$. These values are in good agreement with the earlier paper [22]. Refined atomic coordinates and isotropic thermal displacement parameters are given in Table I. All the crystallographic sites are fully occupied.

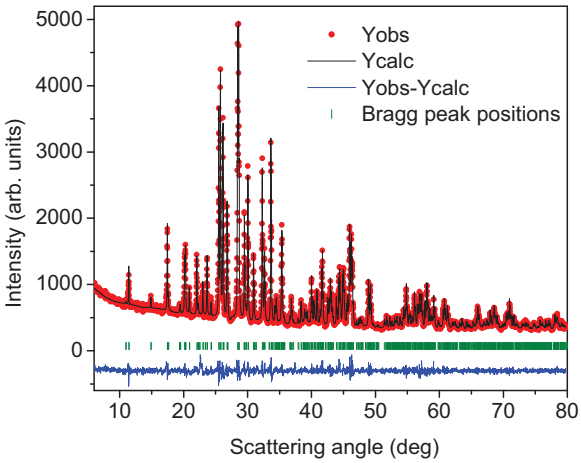

FIG. 1. Rietveld refined x-ray (CuK_α) powder diffraction pattern for $Ba_2Ni(PO_4)_2$ at room temperature. The observed and calculated patterns are shown by the filled circles and solid black line, respectively. The difference between the observed and calculated patterns is shown by the thin line at the bottom. The vertical bars represent the allowed Bragg peak positions.

The crystal structure of $Ba_2Ni(PO_4)_2$ can be represented by layers of NiO_6 octahedra and $(PO_4)^{-3}$ groups. Within a given layer, the NiO_6 octahedra share corners with the PO_4 tetrahedra, producing a honeycomb arrangement of the magnetic Ni^{2+} ions [Figs. 2(a) and 2(b)]. One such honeycomb unit of the Ni^{2+} ions is marked by the dashed rounded line in Fig. 2(a), and its details are shown in Fig. 2(b). The honeycomb units of the NiO_6 octahedra form buckled honeycomb planes as shown in Fig. 2(c). The buckled honeycomb layers are also connected along the crystallographic a axis by the PO_4 tetrahedra resulting in a zigzag chain structure [Fig. 2(e)]. The barium (Ba) atoms are situated between the honeycomb layers [Fig. 2(a)]. All the magnetic Ni^{2+} ions are crystallographically identical and located within the NiO_6 octahedra. On the

TABLE I. Fractional atomic coordinates and isotropic thermal parameters (B_{iso}, in Å^{-2}) obtained from the Rietveld refinement at room temperature. The goodness of fit is $\chi^2 = 1.66$. For atoms of each type, thermal displacement parameters were refined as a single parameter. All atoms occupy $4e$ crystallographic sites, and all the atomic sites are found to be fully occupied. The numbers in the parentheses are the respective error bars.

Atom	x/a	y/b	z/c	B_{iso}
Ba1	0.2969(6)	0.2974(3)	0.9820(2)	0.76(4)
Ba2	0.7421(6)	0.8469(3)	0.2696(2)	0.76(4)
Ni	0.2763(18)	0.4873(8)	0.3640(5)	1.06(17)
P1	0.7270(2)	0.5846(17)	0.4190(8)	0.92(20)
P2	0.2400(2)	0.6075(16)	0.1639(9)	0.92(20)
O11	0.7910(4)	0.5890(2)	0.5168(17)	1.42(8)
O12	0.5110(5)	0.7040(3)	0.4044(15)	1.42(8)
O13	0.6550(5)	0.4410(3)	0.3875(14)	1.42(8)
O14	0.9640(5)	0.6430(3)	0.3764(15)	1.42(8)
O21	0.3570(4)	0.5230(3)	0.0881(15)	1.42(8)
O22	0.3560(5)	0.7570(3)	0.1725(14)	1.42(8)
O23	−0.0330(4)	0.6150(3)	0.1652(13)	1.42(8)
O24	0.3190(5)	0.5340(3)	0.2375(16)	1.42(8)

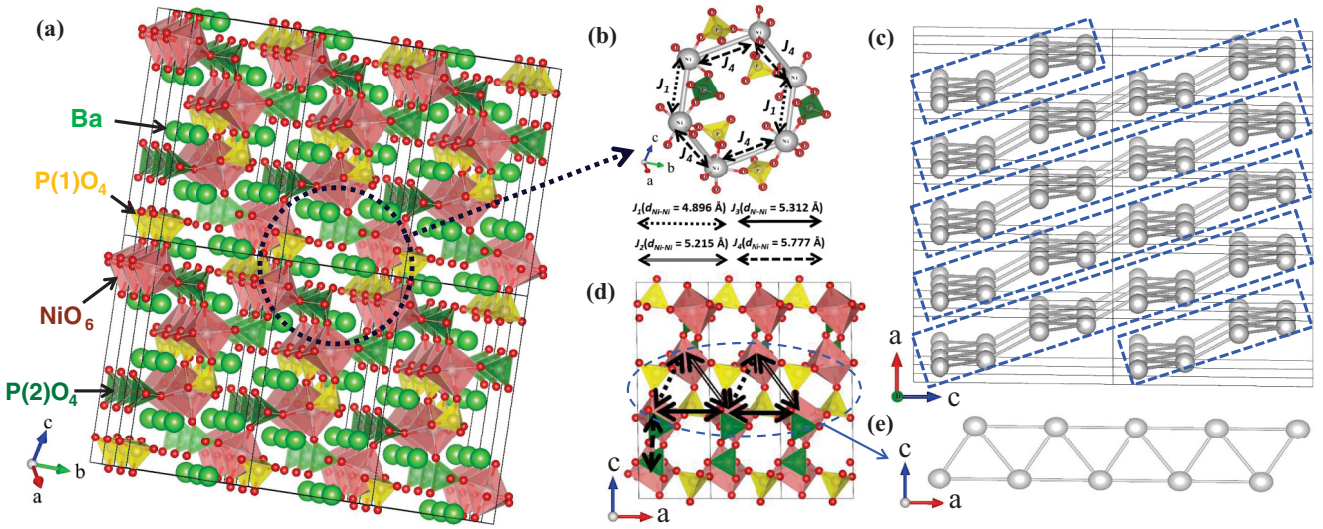

FIG. 2. (a) Overall view of the $Ba_2Ni(PO_4)_2$ crystal structure. The dashed line shows a honeycomb unit formed by NiO_6 octahedra and two nonequivalent $P(1)O_4$ and $P(2)O_4$ tetrahedra. (b) Detailed view of the honeycomb unit with nearest-neighbor exchange interactions. (c) Projection of the crystal structure on the ac plane, where buckled honeycomb planes of Ni^{2+} ions are shown by the dashed rectangular boxes. (d) Projection of the crystal structure on the ac plane showing the zigzag chains along the a axis (perpendicular to the honeycomb planes). (e) Detailed view of the zigzag chains along the a axis.

other hand, phosphorous atoms occupy two inequivalent crystallographic sites, P(1) and P(2), which form nearly regular $P(1)O_4$ and $P(2)O_4$ tetrahedra, respectively.

A schematic diagram of the magnetic interaction geometry is shown in Fig. 3. The honeycomb layers of Ni^{2+} ions are distorted, with two different interaction pathways J_1 and J_4 running via the $P(1)O_4$ and $P(2)O_4$ tetrahedra, respectively, within the honeycomb planes. For each Ni^{2+} ion, there are two interactions of type J_4 and one interaction of type J_1. Additionally, there are two interactions of type J_3 and one interaction of type J_2 between the honeycomb planes.

B. Magnetization

The temperature-dependent dc-magnetic susceptibility $\chi = M/H$ curve measured under $H = 1$ T is presented in Fig. 4(a). With decreasing temperature, the susceptibility curve shows a broad maximum at $T_{max} \sim 8$ K corresponding to the onset of short-range spin-spin correlations. At lower temperatures, the $\chi(T)$ curve exhibits a sharp drop followed by an upturn. The $[d(\chi T)/dT]$ curve for the $H = 0.1$ T shows two magnetic transitions at 5 and 4.6 K identified as T_{N1} and T_{N2}, respectively [Fig. 4(b)]. These transition temperatures are in excellent agreement with the heat-capacity data presented later. Figure 4(c) shows the $\chi(T)$ curves measured under different applied magnetic fields. In higher fields, the low-temperature susceptibility increases, indicating a gradual smearing out of the magnetic transitions.

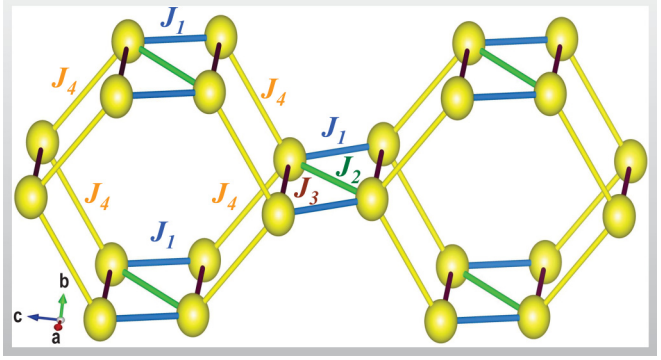

FIG. 3. A schematic diagram of exchange interactions between the Ni^{2+} ions in $Ba_2Ni(PO_4)_2$.

The high-temperature $\chi(T)$ data ($T > 40$ K) measured under an applied field of 1 T follow Curie-Weiss–type behavior [Fig. 4(a)]. To fit the susceptibility data, we used the expression

$$\chi = \chi_0 + \frac{C}{T - \theta_{CW}}, \tag{2}$$

where χ_0 is the temperature-independent contribution that accounts for core diamagnetism and Van Vleck paramagnetism. The second term is the Curie-Weiss law with the Curie constant $C = N_A \mu_{eff}^2 / 3k_B$, where N_A is Avogadro's number, μ_{eff} is the effective magnetic moment, and k_B is the Boltzmann's constant. The parameter θ_{CW} is the Curie-Weiss temperature.

The fit of Eq. (2) to the $\chi^{-1}(T)$ data in the temperature range 40 K $\leqslant T \leqslant$ 280 K gives $\chi_0 = -2.192(4) \times 10^{-4}$ cm^3/mol-Ni^{2+}, $C = 1.433(2)$ cm^3 K/mol $-$ Ni^{2+}, and $\theta_{CW} = -10.423(2)$ K. The negative value of θ_{CW} indicates predominant AFM interactions in $Ba_2Ni(PO_4)_2$. The effective magnetic moment (μ_{eff}) is calculated to be $3.386(2)\mu_B$/Ni^{2+}, which is larger than the expected spin-only value of $2.83\,\mu_B$/Ni^{2+} for the $S = 1$ and $g = 2$. The higher value of μ_{eff} is in agreement with the previous report for $BaNi_2(PO_4)_2$ [22] and $SrNi_2(PO_4)_2$ [22,30]. For the studied compound $Ba_2Ni(PO_4)_2$, the derived μ_{eff} value corresponds to $g = 2.33$ indicating a sizable contribution of the orbital moment due to spin-orbit coupling.

The isothermal magnetization M versus H curves measured at 1.9 and 10 K are shown in the main panel of Fig. 5, the

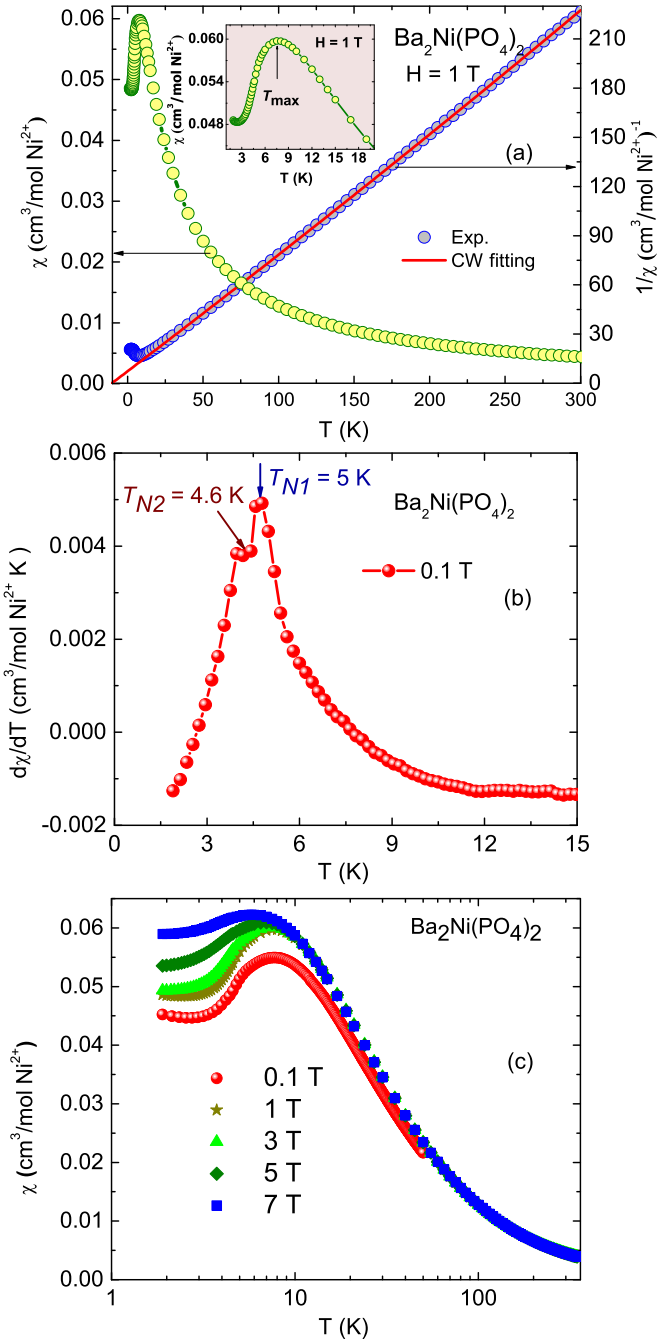

FIG. 4. (a) Temperature-dependent dc-magnetic susceptibility ($\chi = M/H$) and inverse magnetic susceptibility χ^{-1} of $Ba_2Ni(PO_4)_2$ measured under an applied magnetic field of $H = 1$ T. The straight solid red line is the linear fit to the $\chi^{-1}(T)$ data (40 K $\leqslant T \leqslant$ 280 K) and we extrapolated the curve over -10.42 K $\leqslant T \leqslant$ 300 K. The $\chi(T)$ curve in the low-T region (1 K $\leqslant T \leqslant$ 20 K) is shown in the inset. (b) The $d(\chi T)/dT$ versus T curve, measured under $H = 0.1$ T over the low-T region. (c) The $\chi(T)$ curves measured under different applied magnetic fields.

inset shows the isothermal magnetization curves measured at various temperatures. At the lowest measured temperature of 1.9 K, the behavior of the magnetization without any hysteresis suggests an AFM ground state. The magnetization does not saturate up to 14 T and the value of $M \sim 1.3\mu_B/\mathrm{Ni}^{2+}$ at 14 T

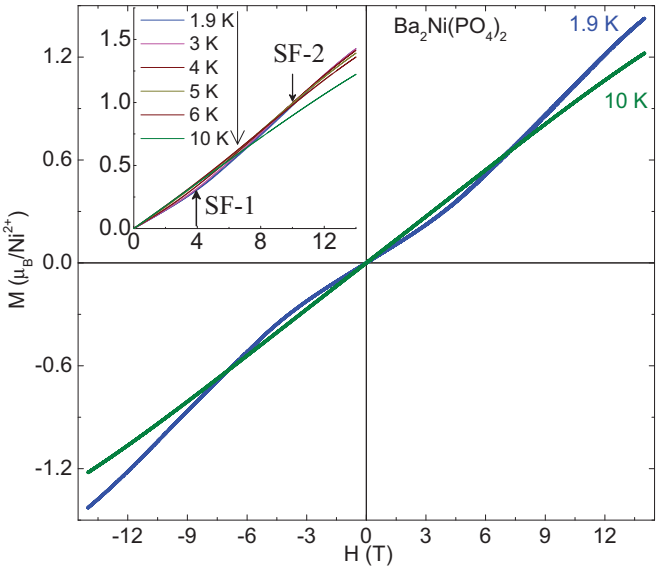

FIG. 5. Magnetization (M) as a function of the applied field (H) measured at 1.9 and 10 K. The inset shows the M vs H curves at various temperatures, and field-induced transitions are marked by SF-1 and SF-2.

is much smaller than the expected saturated magnetic moment of $M_s = gS\mu_B = 2.33\mu_B/\mathrm{Ni}^{2+}$, where we used $S = 1$ and $g = 2.33$ from the Curie-Weiss fit. The magnetization curves measured below 5 K demonstrate a clear upward curvature corresponding to a field-induced spin-flop transition at $H \sim 4$ T. A careful inspection of the dM/dH curve (Fig. 6) confirms the spin-flop transition around 4 T. Additionally, a change in the slope seen around 10 T can be tentatively ascribed to another field-induced phase transition in $Ba_2Ni(PO_4)_2$.

C. Heat capacity

The results of the heat-capacity versus temperature measurements under different magnetic field, performed on a

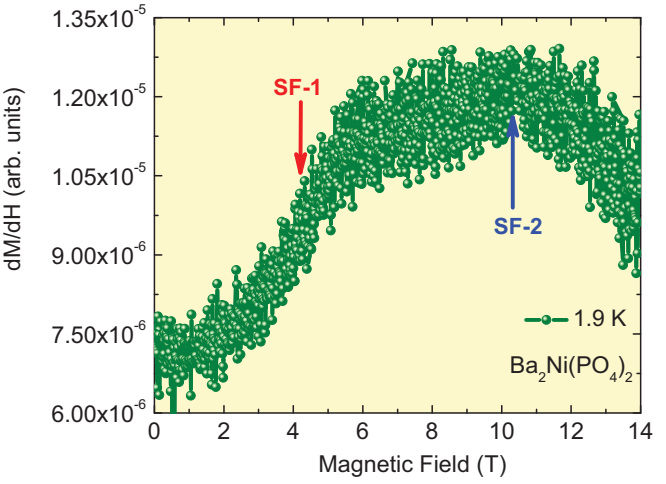

FIG. 6. dM/dH vs H curve at 1.9 K showing two pronounced kinks at around 4 and 10 T, respectively. These transitions are labeled by the down arrow (SF-1) and up arrow (SF-2), respectively.

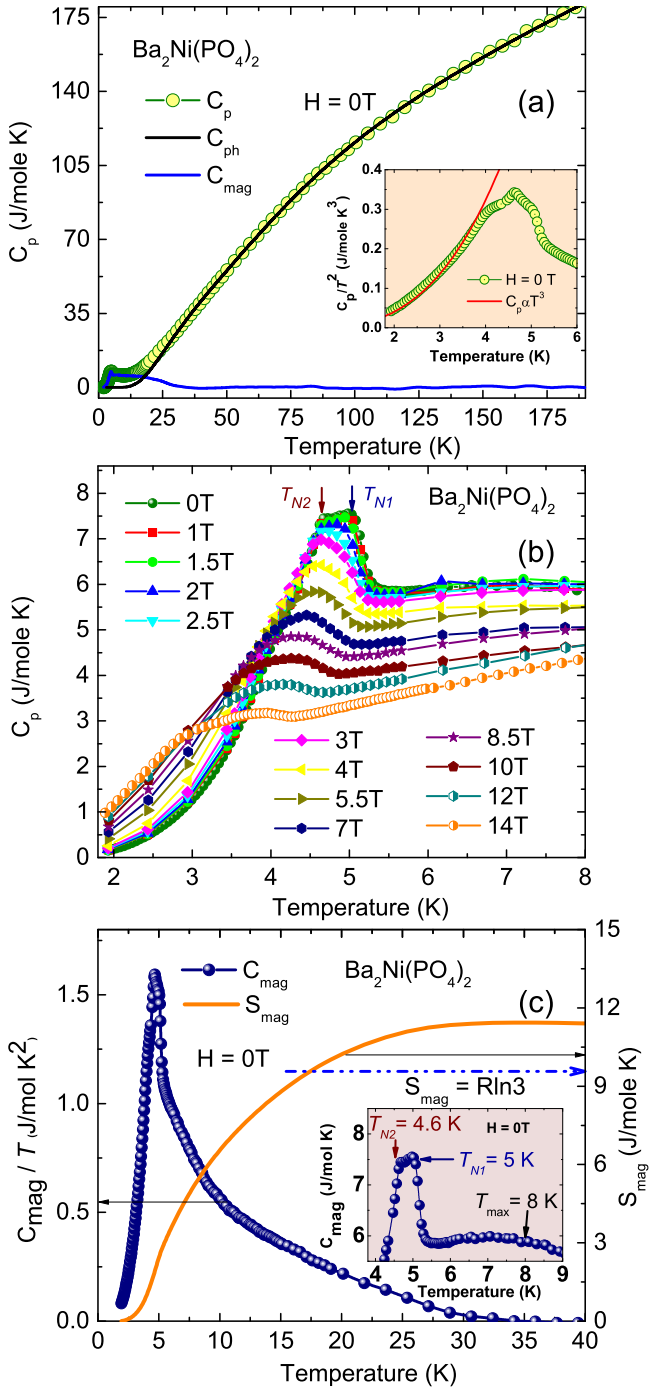

FIG. 7. (a) Temperature dependence of the specific heat C_p of $Ba_2Ni(PO_4)_2$ measured at zero field. Open circles are the raw data, the solid black line shows the phonon contribution C_{ph} [according to the fit with Eq. (3)], and the solid blue line indicates the magnetic contribution. The inset shows the T^3 dependence of the heat capacity below T_N. (b) The heat capacity of $Ba_2Ni(PO_4)_2$ measured at different applied magnetic fields. The arrows denote T_{N1} and T_{N2}. (c) The C_{mag} as a function of temperature over the low-temperature range (1.5–40 K). The calculated magnetic entropy (S_{mag}) (solid orange line) as a function of temperature. Inset shows the C_{mag} curve zoomed over 4–9 K.

small pressed pellet of $Ba_2Ni(PO_4)_2$ using the relaxation technique, are shown in Fig. 7. In agreement with the magnetic susceptibility results, zero-field heat-capacity curve reveals two successive magnetic transitions at $T_{N1} = 5$ K and $T_{N2} = 4.6$ K, respectively.

Above T_{N1}, a broad peak due to short-range magnetic ordering is apparent around 8 K [inset of Fig. 7(c)]. This peak is suppressed under the applied magnetic field. The transitions at T_{N1} and T_{N2} are suppressed by the field too and shift towards lower temperatures. Above 4 T, only one transition is discernible, which indicates that the two transitions merge around this point. At higher fields, this single transition is suppressed further. This is consistent with the susceptibility results depicted in Fig. 4(c).

In order to estimate the magnetic contribution to the specific heat, we proceed as follows: first, we approximate the lattice contribution C_{ph} by fitting the data above 20 K with a superposition of one Debye-type and three Einstein-type terms according to [31,32]

$$C_{ph}(T) = f_D C_{Deb}(\Theta_{Deb}, T) + \sum_{i=1}^{3} g_i C_{Ein,i}(\Theta_{Ein,i}, T). \quad (3)$$

The Debye-type heat capacity is given by

$$C_{Deb}(T) = 9R\left(\frac{T}{\Theta_{Deb}}\right)^3 \int_0^{\Theta_{Deb}/T} \frac{x^4 e^x}{(e^x - 1)^2}\, dx. \quad (4)$$

In order to simplify the fitting procedure, a Padé approximant for the Debye-type heat capacity, proposed recently by Goetsch *et al.* [33], was utilized. The Einstein-type heat capacities $C_{Ein,i}(T)$ were calculated according to

$$C_{Ein,i}(T) = 3R\left(\frac{\Theta_{Ein,i}}{T}\right)^2 \frac{\exp(\Theta_{Ein,i}/T)}{[\exp(\Theta_{Ein,i}/T) - 1]^2}, \quad (5)$$

where R is the universal gas constant, k_B is the Boltzmann constant, Θ_{Deb} and Θ_{Ein} are the Debye and Einstein temperatures, respectively. In the Debye-Einstein model, the total number of modes n is equal to the total number of atoms in the formula unit. For $Ba_2Ni(PO_4)_2$ this number is 13. We considered the ratio of the relative weights of the Debye and Einstein modes to be $1 : (n - 1)$. During the fitting of the specific-heat data by the Einstein-Debye phonon model we have found that the higher-order Einstein terms (beyond the third term) remain close to zero and render the fitting procedure unstable. A model with a combination of one Debye term and three Einstein terms fits the observed data well in the temperature range 20–200 K, as shown in Fig. 7(a). This model is empirical in nature. It could be refined if further information on lattice dynamics of $Ba_2Ni(PO_4)_2$ were available. The fitting results are presented in Table II.

TABLE II. Relative weights and characteristic temperatures Θ used to approximate lattice contribution to the heat capacity of $Ba_2Ni(PO_4)_2$ according to Eq. (3).

Contribution	Weight	Θ (K)
Debye, $i = 1$	0.0769	714.5(5)
Einstein, $i = 1$	0.3159	323.1(2)
Einstein, $i = 2$	0.2229	113.5(8)
Einstein, $i = 3$	0.3843	1012(2)

By subtracting $C_{\rm ph}$ from the experimental heat capacity, we obtain the magnetic contribution $C_{\rm mag}$. A plot of $C_{\rm mag}(T)/T$ versus T is shown in Fig. 7(c). The associated magnetic entropy is calculated as follows:

$$S_{\rm mag}(T) = \int_0^T \frac{C_{\rm mag}(T')}{T'}\, dT'. \tag{6}$$

We obtain the overall magnetic entropy $S_{\rm mag} = 11.45(1)\ {\rm J\,mol^{-1}\,K^{-1}}$, which is in reasonable agreement with the entropy of a $S = 1$ system, $S_{\rm mag} = R\ln(2S+1) = 9.14\ {\rm J\,mol^{-1}\,K^{-1}}$. The remaining discrepancy may be due to the uncertainties in estimating the lattice part $C_{\rm ph}$.

At low temperatures, magnetic specific heat follows the power-law behavior

$$C_p(T) \propto T^n \tag{7}$$

with $n \sim 3$, as expected for the linear spin-wave dispersion relation in a three-dimensional antiferromagnet is shown in inset of Fig. 7(a).

D. Magnetic ground state

Magnetic ground state of $Ba_2Ni(PO_4)_2$ is investigated by the low-temperature neutron powder diffraction. The measured diffraction patterns at 7 K (paramagnetic state) and 1.5 K (magnetically ordered state) are shown in Figs. 8(a) and 8(b), respectively. The room-temperature monoclinic crystal structure with the space group $P2_1/n$ reproduces the nuclear phase at low temperatures. At 7 K (paramagnetic state), all peaks can be ascribed to the nuclear structure. The lattice parameters at 7 K are found to be $a = 5.2005(3)$ Å, $b = 8.6116(5)$ Å, $c = 15.7423(11)$ Å, and $\beta = 90.72(5)^\circ$ with the unit-cell volume of $V = 705.0(8)$ Å^3.

Figure 8(b) depicts the observed pattern at 1.5 K along with the calculated pattern, where only the nuclear phase of $Ba_2Ni(PO_4)_2$ was assumed. Weak additional peaks at $Q \sim 0.64$ Å^{-1} and 0.97 Å^{-1} have magnetic origin. The temperature dependence of the magnetic peak at $Q \sim 0.97$ Å^{-1} is shown in the inset of Fig. 8(b). The pure magnetic pattern at 1.5 K is estimated after subtraction of the nuclear background at 7 K and depicted in Fig. 8(c). All magnetic peaks can be indexed with the propagation vector $\mathbf{k} = (\frac{1}{2}, 0, \frac{1}{2})$ with respect to the monoclinic unit cell.

To determine magnetic structures compatible with the symmetry of $Ba_2Ni(PO_4)_2$, we performed representation analysis using the BASIREPS program available in the FULLPROF suite [25]. Representational analysis determines those magnetic structures that can be formed upon a second-order phase transition. The crystal structure in the paramagnetic state and the propagation vector of the magnetic ordering are used as input. The analysis involves the determination of space-group symmetry elements that leave the propagation vector $\mathbf{k}$ invariant. These symmetry elements form a little group $G_{\mathbf{k}}$. The magnetic representation for a given magnetic site is then decomposed in terms of the irreducible representations (IRs) of the little group $G_{\mathbf{k}}$ as follows:

$$\Gamma_{\rm mag} = \sum_\nu n_\nu \Gamma_\nu^\mu, \tag{8}$$

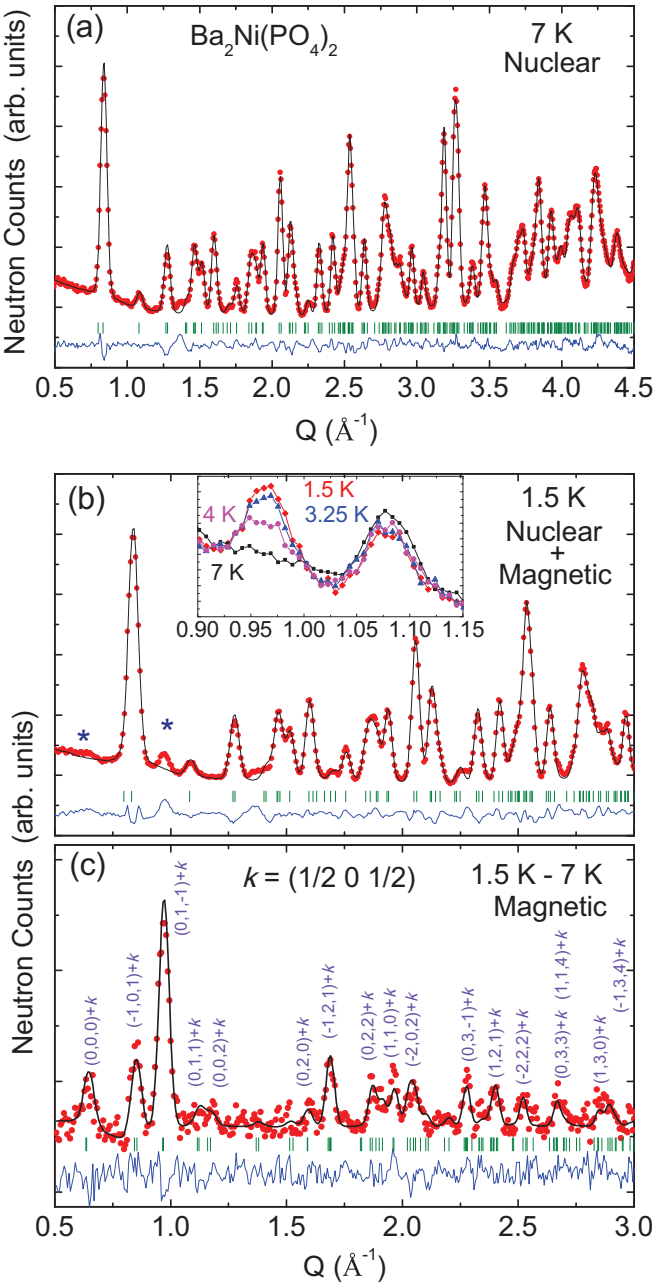

FIG. 8. Experimentally observed (circles) and calculated (solid black lines) neutron diffraction patterns for $Ba_2Ni(PO_4)_2$ at (a) 7 K (paramagnetic state) and (b) 1.5 K (magnetically ordered state), respectively. (c) Experimental magnetic pattern (red circles) at 1.5 K (after subtraction of the nuclear background at 7 K). The magnetic pattern is calculated (black solid line) as per the Γ_2. The inset of (b) shows temperature dependence of the strongest magnetic Bragg peak at $Q \sim 0.97$ Å^{-1}. The magnetic pattern in (c) is zoomed vertically for clarity. The solid blue lines at the bottom of each panel represent the difference between the observed and calculated patterns. The vertical bars indicate the positions of the nuclear and magnetic Bragg peaks allowed by symmetry.

where Γ_ν^μ is the IR of order μ, and n_ν shows how many times it appears in the magnetic representation $\Gamma_{\rm mag}$ for a given crystallographic site. The number of "symmetry-allowed" magnetic structures possible for a given crystallographic site

TABLE III. Irreducible representations of the group $G_{\mathbf{k}}$ of the propagation vector $\mathbf{k} = (\frac{1}{2},0,\frac{1}{2})$ for $Ba_2Ni(PO_4)_2$.

	Symmetry element of G_k			
IRs	$\{E\|000\}$	$\{C_{2y}\|0.50.50.5\}$	$\{I\|000\}$	$\{\sigma_y\|0.50.50.5\}$
Γ_1^1	1	1	1	1
Γ_2^1	1	1	−1	−1
Γ_3^1	1	−1	1	−1
Γ_4^1	1	−1	−1	1

is simply the number of nonzero IRs in the decomposition of its magnetic representation.

The space group of $Ba_2Ni(PO_4)_2$ involves four symmetry operations ($\{E|000\}$, $\{C_{2y}|0.50.50.5\}$, $\{I|000\}$, and $\{\sigma_y|0.50.50.5\}$). All of them leave the propagation vector $\mathbf{k} = (\frac{1}{2},0,\frac{1}{2})$ invariant. For this propagation vector, the irreducible representations (IRs) of the little group $G_{\mathbf{k}}$ are given in Table III. There are four possible IRs, which are all one dimensional. The reducible magnetic representation Γ_{mag} for the Ni site can be decomposed as a direct sum of the IRs as follows:

$$\Gamma_{\text{mag}}^{\text{Ni}} = 3\Gamma_1^1 + 3\Gamma_2^1 + 3\Gamma_3^1 + 3\Gamma_4^1. \quad (9)$$

The basis vectors (the Fourier components of the magnetization) for the magnetic Ni site are given in Table IV. These basis vectors are calculated using the projection operator technique implemented in BASIREPS.

For a second-order magnetic transition, only one representation can be involved according to the Landau theory. The number of degrees of freedom to be refined is reduced to the number of basis vectors associated with the given IR. For $Ba_2Ni(PO_4)_2$, there are four possible magnetic structures: Γ_1, Γ_2, Γ_3, and Γ_4. Each of them is one dimensional and repeated three times in Eq. (9). There are three basis vectors corresponding to each of these representations and, therefore, three refinable parameters. The magnetic structure for $Ba_2Ni(PO_4)_2$ can be represented by one of these IRs.

TABLE IV. Basis vectors of the magnetic Ni site with the propagation vector $\mathbf{k} = (\frac{1}{2},0,\frac{1}{2})$ for $Ba_2Ni(PO_4)_2$. Only real components of the basis vectors are presented. The atoms of the nonprimitive basis are defined according to Ni1: (x,y,z), Ni2: $(\bar{x}+\frac{1}{2},y+\frac{1}{2},\bar{z}+\frac{1}{2})$, Ni3: $(\bar{x},\bar{y},\bar{z})$, and Ni4: $(x+\frac{1}{2},\bar{y}+\frac{1}{2},z+\frac{1}{2})$, where $x = 0.2763$, $y = 0.4873$, and $z = 0.3640$.

		Basis vectors			
IRs		Ni1	Ni2	Ni3	Ni4
Γ_1^1	Ψ_1	(100)	$(\bar{1}00)$	(100)	$(\bar{1}00)$
	Ψ_2	(010)	(010)	(010)	(010)
	Ψ_3	(001)	$(00\bar{1})$	(001)	$(00\bar{1})$
Γ_2^1	Ψ_1	(100)	$(\bar{1}00)$	$(\bar{1}00)$	(100)
	Ψ_2	(010)	(010)	$(0\bar{1}0)$	$(0\bar{1}0)$
	Ψ_3	(001)	$(00\bar{1})$	$(00\bar{1})$	(001)
Γ_3^1	Ψ_1	(100)	(100)	(100)	(100)
	Ψ_2	(010)	$(0\bar{1}0)$	(010)	$(0\bar{1}0)$
	Ψ_3	(001)	(001)	(001)	(001)
Γ_4^1	Ψ_1	(100)	(100)	$(\bar{1}00)$	$(\bar{1}00)$
	Ψ_2	(010)	$(0\bar{1}0)$	$(0\bar{1}0)$	(010)
	Ψ_3	(001)	(001)	$(00\bar{1})$	$(00\bar{1})$

The refinement of the magnetic structure was attempted for all the four Γ's. Only Γ_1 and Γ_2 reproduce the experimental magnetic pattern at 1.5 K. Both Γ_1 and Γ_2 produce fits of similar quality ($R_{\text{mag}} = 11.8\%$ and 11.7%, respectively) [Fig. 8(c)]. The difference between these two magnetic structures is the arrangement of the spin component m_b along the b axis. The m_b spin components for Γ_1 arrange parallel to each other, whereas the m_b's are antiparallel in the case of Γ_2 (Table IV). While the refined value of m_b is within the error bar for both Γ_1 and Γ_2, there is no symmetry argument that would exclude m_b entirely. Therefore, the magnetic structure determined within Γ_1 should be weakly ferromagnetic at odds with the experiment, where $M(H)$ is linear in low fields, and no signatures of net magnetization or hysteresis are observed (Fig. 5). We thus conclude that only Γ_2 provides the correct solution. Moreover, the resulting magnetic structure according to the Γ_2 is in agreement with our microscopic analysis reported below (Sec. III F).

The basis vectors for Γ_2 (Table IV) indicate that all three components of the magnetic moment are refinable. Their simultaneous refinement yields $m_a = 0.22(6)\mu_B$, $m_b = -0.11(8)\mu_B$, and $m_c = 1.73(3)\mu_B$ with the total magnetic moment $m = 1.75(8)\mu_B$ at 1.5 K. The obtained values indicate that the spins are lying in the ac plane with a predominating component along the c axis. This ordered moment is about 10 % smaller than the spin-only ordered moment of $2\,\mu_B$ for $S = 1$ and 25% smaller than the full moment of $gS\mu_B = 2.33\ \mu_B$ expected for $g = 2.33$ when the contribution of the orbital moment is included, for this sample.

The resulting magnetic structure (corresponding to the magnetic ground state at $T \leqslant T_{N2}$) is shown in Fig. 9. It can be identified as stripe AFM order because each spin in the honeycomb plane is surrounded by two spins having the opposite directions and one spin having the same direction, so that stripes along the b direction are formed. The order along a is simple AFM. This magnetic structure is fairly rare

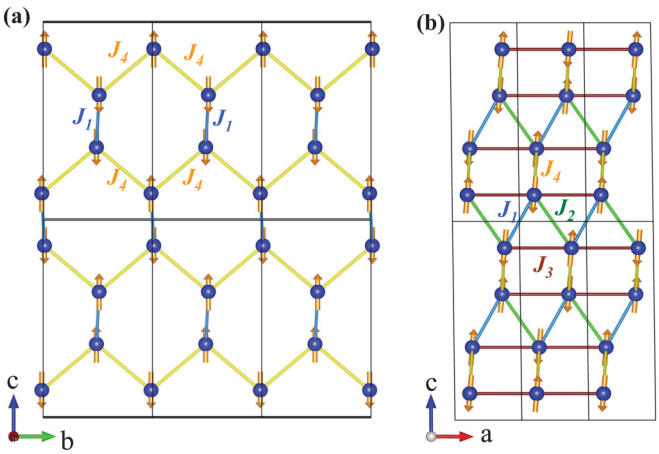

FIG. 9. The magnetic structure of $Ba_2Ni(PO_4)_2$. The projections of the magnetic structure in the (a) bc and (b) ac planes, respectively. (Figures 2 and 9 were prepared using the VESTA software [43].)

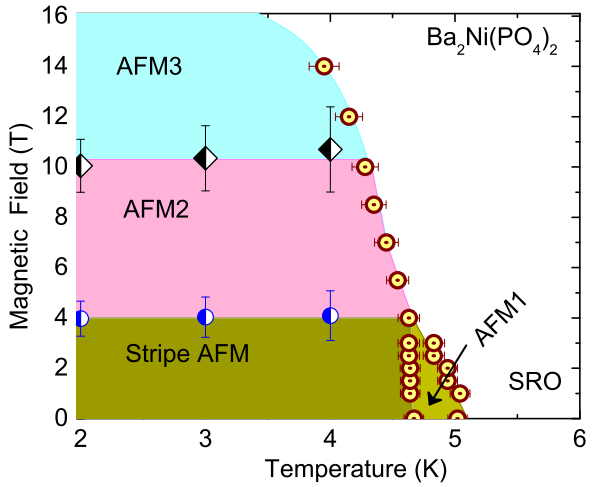

FIG. 10. Magnetic phase diagram of $Ba_2Ni(PO_4)_2$ in the H-T plane. The half-filled and open circles with central dot points are obtained from magnetization and heat-capacity measurements, respectively.

among Ni^{2+}-based honeycomb systems. For example, $NiPS_3$ [16], $Na_3Ni_2BiO_6$ [18], and $Cu_3Ni_2SbO_6$ [17] all show zigzag antiferromagnetic order, and only $KNiAsO_4$ [20] reveals a stripe phase equivalent to the one in the studied compound $Ba_2Ni(PO_4)_2$.

E. Magnetic phase diagram

The susceptibility, magnetization, heat-capacity, and neutron diffraction data were used to sketch a temperature-field phase diagram of $Ba_2Ni(PO_4)_2$ (Fig. 10). In zero field, two consecutive magnetic transitions are observed. The values of T_{N1} and T_{N2} are determined form the peak positions of the C_p versus T curves [at the point where the derivative curve $d(C_p)/dT$ changes its sign] which are used for the construction of the magnetic phase diagram. The error bars are calculated from the temperature range over which a change of $\pm 3\%$ of $d(C_p)/dT$ value is observed. The ordered state below T_{N2} is identified as stripe AFM order with spins pointing approximately along the c direction, as revealed by the neutron diffraction data. The AFM1 state, formed in the narrow temperature range between T_{N1} and T_{N2}, has not been characterized in detail, and requires further investigation. In this study, no neutron diffraction pattern was measured in the AFM1 phase. We emphasize that the microscopic nature of the AFM1 state could be resolved by neutron diffraction.

The horizontal line around 4 T is naturally ascribed to a spin-flop transition, where spins align perpendicular to the applied field. Therefore, AFM2 is likely the spin-flop version of the stripe AFM phase. Another anomaly is evident around 10 T in the dM/dH curve (Fig. 6) which is tentatively assigned to the second field-induced transition. Its origin requires further investigation.

F. Microscopic magnetic model

Electronic structure of $Ba_2Ni(PO_4)_2$ is typical for a magnetic insulator. LDA calculations produce metallic solution caused by the underestimation of strong correlations in the Ni $3d$ shell (Fig. 11). The anticipated insulating state is well reproduced on the LSDA+U level, where we find the band gap of 3.56 eV and magnetic moments of about $1.9\mu_B$. Ni $3d$ states are split into the t_{2g} and e_g manifolds, as expected in the octahedral crystal field. In the LDA band structure, the Fermi level crosses the e_g bands, so that $\alpha = 3z^2 - r^2$ and $\beta = x^2 - y^2$ are magnetic orbitals (Fig. 11).

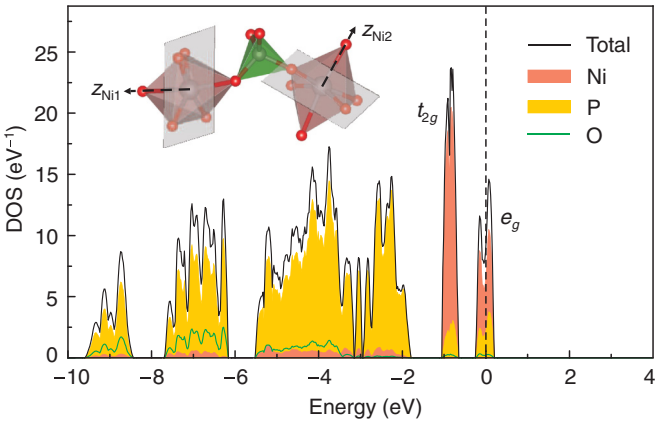

FIG. 11. LDA band structure for $Ba_2Ni(PO_4)_2$, the Fermi level is at zero energy. Note the clear separation of the Ni $3d$ states into the t_{2g} and e_g manifolds. The inset shows distinct easy planes of two neighboring Ni atoms.

Exchange couplings in $Ba_2Ni(PO_4)_2$ were computed using total energies of collinear spin configurations obtained on the LSDA+U level [34]. All calculations were performed in the supercell doubled along the a direction, such that four relevant couplings J_1-J_4 could be resolved. Additionally, we consider the hoppings t_i between the e_g states in the LDA band structure. These hoppings underlie the superexchange process ($J_i \sim t_i^2$) and allow for a qualitative assessment of the magnetic couplings in $Ba_2Ni(PO_4)_2$.

Exchange couplings in $Ba_2Ni(PO_4)_2$ are listed in Table V. The values of J_i correlate with individual hopping parameters. For example, the smallest hopping probabilities for J_1 ($t_i \leqslant 26$ meV) result in the weaker coupling, whereas the largest hopping $t_3^{\beta\alpha} = -65$ meV triggers the strongest exchange coupling J_3. Regarding the absolute scale, all exchange couplings are relatively weak because NiO_6 octahedra are separated by PO_4 tetrahedra, and the Ni-Ni distances are quite long.

TABLE V. Magnetic exchange couplings in $Ba_2Ni(PO_4)_2$. The interatomic distances $d_{Ni\text{-}Ni}$ are given in Å. The hopping parameters t_i (in meV) are obtained from the LDA band structure, whereas $\alpha = 3z^2 - r^2$ and $\beta = x^2 - y^2$ denote orbital indices. Full exchange couplings J_i (in K) are calculated on the LSDA+U level, as described in the text. All exchange couplings J_i are antiferromagnetic in nature.

		t_i				
	$d_{Ni\text{-}Ni}$	$\alpha\alpha$	$\alpha\beta$	$\beta\alpha$	$\beta\beta$	J_i
J_1	4.896	15	26	26	21	0.5
J_2	5.215	−6	−3	−3	44	1.3
J_3	5.312	34	−15	−65	18	3.5
J_4	5.777	38	6	45	1	1.8

For interaction pathways beyond nearest neighbors, all hopping parameters t_i are below 4 meV, suggesting that the respective exchange couplings are much weaker than J_1-J_4 listed in Table V and can be safely neglected in the microscopic analysis. Exchange couplings in Table V are also consistent with the stripe AFM order observed experimentally. Its formation is triggered by the coupling J_2 that is oblique to the honeycomb planes and overrides J_1, which runs within the honeycomb planes. The couplings J_3 and J_4 are compatible with the stripe order. Our computed exchange couplings can be juxtaposed with the experimental Curie-Weiss temperature $\theta_{\rm CW} = -10.4$ K. We estimate it as follows:

$$\theta_{\rm CW} = -\frac{S(S+1)}{3}\sum_i z_i J_i, \tag{10}$$

where the number of neighbors is $z_i = 1$ for J_1 and J_2 and $z_i = 2$ for J_3 and J_4. We find $\theta_{\rm CW} = -8.3$ K.

In the following, we analyze the effects of magnetic anisotropy. They are rooted in the structure of orbital levels of Ni^{2+}. In $Ba_2Ni(PO_4)_2$, the NiO_6 octahedra are distorted, with five shorter Ni-O distances of 2.04–2.07 Å and one longer distance of 2.31 Å. This longer Ni-O bond defines the direction of the local z axis (same convention has been used for the orbital indices α and β in Table V).[1] The energies of the e_g orbitals are $\varepsilon_{x^2-y^2} = 0.003$ eV and $\varepsilon_{3z^2-r^2} = -0.030$ eV, in line with simple geometrical arguments suggesting that the extended Ni-O distance along the local z direction will stabilize the $3z^2 - r^2$ orbital and destabilize the $x^2 - y^2$ orbital. However, an opposite trend is seen for the t_{2g} states, where $\varepsilon_{xy} = -0.895$ eV is lower than $\varepsilon_{xz} = -0.816$ eV and $\varepsilon_{yz} = -0.814$ eV. This discrepancy can be ascribed to a rather complex distortion of the NiO_6 octahedron, where the xy plane is deformed, and one of the out-of-plane Ni-O bonds forms an angle of 70° with this plane instead of 90° expected in a regular octahedron.

For Ni^{2+} ions, single-ion anisotropy can be estimated using second-order perturbation theory for the spin-orbit coupling [35,36]:

$$\begin{aligned} A_x &= \left(\frac{\lambda}{2}\right)^2\left(\frac{1}{\varepsilon_{x^2-y^2}-\varepsilon_{yz}} + \frac{3}{\varepsilon_{3z^2-r^2}-\varepsilon_{yz}}\right), \\ A_y &= \left(\frac{\lambda}{2}\right)^2\left(\frac{1}{\varepsilon_{x^2-y^2}-\varepsilon_{xz}} + \frac{3}{\varepsilon_{3z^2-r^2}-\varepsilon_{xz}}\right), \\ A_z &= \left(\frac{\lambda}{2}\right)^2\left(\frac{4}{\varepsilon_{x^2-y^2}-\varepsilon_{xy}}\right), \end{aligned} \tag{11}$$

where $\lambda = 0.078$ eV is the spin-orbit coupling constant for Ni^{2+} [37]. This way, we obtain $A_x = 89.6$ K, $A_y = 89.4$ K, and $A_z = 79.0$ K corresponding to an effective easy-plane anisotropy $A = A_z - (A_x + A_y)/2 = -10.5$ K [see Eq. (1)] with xy as the magnetic easy plane. The easy-plane type of magnetic anisotropy is rooted in the distortion of the NiO_6 octahedron that renders the nearly degenerate xz and yz states and the xy state with a distinctly different energy.

[1]More precisely, we define $x = [0.1707, \pm 0.0479, 0.0018]$ and $z = [-0.0691, \pm 0.1022, -0.0153]$, where + and − stand for the Ni1/Ni3 and Ni2/Ni4 sites, respectively (see also Table IV).

The orientation of the easy plane with respect to the global crystallographic axes changes upon going from Ni1 and Ni3 to Ni2 and Ni4 following the symmetry of the $Ba_2Ni(PO_4)_2$ structure. By a simple energy minimization, we find that such noncoplanar easy-plane anisotropies should produce preferred spin direction approximately along $[\bar{1}01]$, whereas the a and b directions of the structure are least favorable. This result is compatible with the experimental spin direction along c (i.e., [001]), although there remains a discrepancy that can be remedied by full-relativistic (LSDA+U+SO) calculations. These calculations yield the lowest energy when spins are along c, an intermediate energy for spins along a, and the highest energy for spins along b. The departure of the preferred spin direction from $[\bar{1}01]$ toward [001] is likely due to effects such as Dzyaloshinsky-Moriya interactions that were not included in our model analysis. A detailed anisotropic physical property measurement on a single crystal could shed more light on anisotropic magnetic behavior of $Ba_2Ni(PO_4)_2$.

IV. DISCUSSION AND SUMMARY

$Ba_2Ni(PO_4)_2$ features a honeycomblike geometry of the spin lattice and reveals stripe AFM order, which is rarely seen in honeycomb antiferromagnets. In an isotropic (Heisenberg) honeycomb magnet, stabilization of the stripe order requires that third-neighbor couplings are ferromagnetic [3,20,38], but long-range ferromagnetic couplings are very uncommon in insulators. In $Ba_2Ni(PO_4)_2$, the formation of the stripe order is due to interplane couplings. Our microscopic analysis shows that J_1, one of the nearest-neighbor couplings within the honeycomb plane, is overridden by the interplane coupling J_2. Another coupling between the honeycomb planes J_3 is even stronger than all couplings within the plane, and leads the hierarchy of the J_i values (Table V). $Ba_2Ni(PO_4)_2$ could be viewed as a system of spin-1 Haldane chains stacked on a honeycomb lattice. However, magnetic behavior of this compound is much more involved than in standard spin-chain systems.

Our thermodynamic measurements identify two consecutive phase transitions in zero field at $T_{N1} = 5.0$ K and $T_{N2} = 4.6$ K. A broad maximum around 8 K in the magnetic susceptibility and magnetic specific heat indicates that short-range order precedes long-range magnetic order, and transition toward the long-range-ordered state is impeded, as seen from the ratio $\theta/T_{N1} = 2.08$. In antiferromagnets, long-range order can be impeded because of the competition between isotropic exchange couplings or as a result of the proximity to the dimerized gapped state, which would be formed when spin-1 (Haldane) chains are isolated or weakly coupled (i.e., $J_3 \gg J_1, J_2, J_4$). Neither of these scenarios applies to $Ba_2Ni(PO_4)_2$, though.

Frustration is restricted to the weak coupling $J_1 \simeq 0.5$ K that is several times weaker than the couplings stabilizing the stripe order. Even a stronger frustrating coupling would have little effect on the Néel temperature. For example, in $Li_2NiW_2O_8$, where spin-1 chains are stacked on the frustrated triangular lattice, $\theta/T_{N1} = 1.1$, and the magnetic order sets in already at a temperature $T_{N1} \simeq S(S+1)J_{1D} = 2J_{1D}$, where J_{1D} is the coupling along the spin-1 chains [36]. In

contrast, $Ba_2Ni(PO_4)_2$ is characterized by a lower value of $T_{N1}/J_{1D} \simeq 1.4$.

Regarding the proximity to the gapped phase, the ratio $J_\perp/J_{1D} = J_4/J_3 \simeq 0.5$ should place $Ba_2Ni(PO_4)_2$ very far away from the limit of isolated spin chains. In coupled spin-1 chains, long-range magnetic order sets in already at a very low $J_\perp/J_{1D}$ [39–41], and, for example, even $CsNiCl_3$ with its very small ratio $J_\perp/J_{1D} \simeq 0.017$ develops long-range magnetic ordering [42].

We suggest that the magnetic frustration in $Ba_2Ni(PO_4)_2$ is enhanced by the complex single-ion anisotropies, which impede long-range magnetic ordering in this compound. When taken on their own, two distinct easy planes of the Ni^{2+} ions would favor a noncollinear magnetic order that is not compatible with the isotropic couplings J_i. Similar energy scales of the isotropic exchange couplings and noncoplanar single-ion anisotropies imply that both these effects are integral to the physics of $Ba_2Ni(PO_4)_2$. Their remarkable combination awaits detailed theoretical investigation. Additionally, $Ba_2Ni(PO_4)_2$ exhibits several interesting features, including the intermediate AFM1 phase between T_{N1} and T_{N2} and the field-induced phases above 4 T, that would be interesting for future experimental investigation.

In summary, we have shown that $Ba_2Ni(PO_4)_2$ reveals stripe AFM order at low temperatures in zero field and several magnetic transitions along with clear signatures of short-range magnetic order around 8 K. This feature is reminiscent of quantum and frustrated antiferromagnets and contrasts with the three-dimensional interaction topology that can be represented by spin-1 chains stacked on the honeycomblike lattice. While isotropic exchange couplings feature only a weak magnetic frustration, the sizable single-ion anisotropy of easy-plane type competes with collinear magnetic order favored by the isotropic exchange couplings. This peculiar frustration mechanism may be responsible for the intricate physics of $Ba_2Ni(PO_4)_2$.

ACKNOWLEDGMENTS

A.Y. would like to acknowledge TIFR, Mumbai, for the financial support. A.T. would like to acknowledge DAE India for financial support. We are thankful to central measurement facility TIFR, Mumbai, for P-XRD and magnetization measurements. A.A.T. was supported by the Federal Ministry for Education and Research through the Sofja Kovalevskaya Award of Alexander von Humboldt Foundation.

[1] J. Richter, J. Schulenburg, and A. Honecker, *Quantum magnetism* (Springer, Berlin, 2004), Chap. 2, pp. 85–153.

[2] E. V. Castro, N. M. R. Peres, K. S. D. Beach, and A. W. Sandvik, Site dilution of quantum spins in the honeycomb lattice, Phys. Rev. B **73**, 054422 (2006).

[3] J. B. Fouet, P. Sindzingre, and C. Lhuillier, An investigation of the quantum $J_1 - J_2 - J_3$ model on the honeycomb lattice, Eur. Phys. J. B **20**, 241 (2001).

[4] K. Takano, Spin-gap phase of a quantum spin system on a honeycomb lattice, Phys. Rev. B **74**, 140402(R) (2006).

[5] D. J. J. Farnell, R. F. Bishop, P. H. Y. Li, J. Richter, and C. E. Campbell, Frustrated heisenberg antiferromagnet on the honeycomb lattice: A candidate for deconfined quantum criticality, Phys. Rev. B **84**, 012403 (2011).

[6] Z. Zhu, D. A. Huse, and S. R. White, Weak Plaquette Valence Bond Order in the $S = 1/2$ Honeycomb $J_1 - J_2$ Heisenberg model, Phys. Rev. Lett. **110**, 127205 (2013).

[7] R. Ganesh, J. van den Brink, and S. Nishimoto, Deconfined Criticality in the Frustrated Heisenberg Honeycomb Antiferromagnet, Phys. Rev. Lett. **110**, 127203 (2013).

[8] A. Kitaev, Anyons in an exactly solved model and beyond, Ann. Phys. (NY) **321**, 2 (2006).

[9] J. Xu, A. Assoud, N. Soheilnia, S. Derakhshan, H. L. Cuthbert, J. E. Greedan, M. H. Whangbo, and H. Kleinke, Synthesis, structure, and magnetic properties of the layered copper(II) oxide $Na_2Cu_2TeO_6$, Inorg. Chem. **44**, 5042 (2005).

[10] Y. Miura, R. Hirai, Y. Kobayashi, and M. Sato, Spin-gap behavior of $Na_3Cu_2SbO_6$ with distorted honeycomb structure, J. Phys. Soc. Jpn. **75**, 084707 (2006).

[11] E. Climent-Pascual, P. Norby, N. H. Andersen, P. W. Stephens, H. W. Zandbergen, J. Larsen, and R. J. Cava, Spin-1/2 delafossite honeycomb compound Cu_5SbO_6, Inorg. Chem. **51**, 557 (2012).

[12] S. Derakhshan, H. L. Cuthbert, J. E. Greedan, B. Rahaman, and T. Saha-Dasgupta, Electronic structures and low-dimensional magnetic properties of the ordered rocksalt oxides $Na_3Cu_2SbO_6$ and $Na_2Cu_2TeO_6$, Phys. Rev. B **76**, 104403 (2007).

[13] Y. Miura, Y. Yasui, T. Moyoshi, M. Sato, and K. Kakurai, Magnetic excitations of spin-gap system $Na_3Cu_2SbO_6$ with distorted honeycomb structure, J. Phys. Soc. Jpn. **77**, 104709 (2008).

[14] M. Schmitt, O. Janson, S. Golbs, M. Schmidt, W. Schnelle, J. Richter, and H. Rosner, Microscopic magnetic modeling for the $S = \frac{1}{2}$ alternating-chain compounds $Na_3Cu_2SbO_6$ and $Na_2Cu2TeO_6$, Phys. Rev. B **89**, 174403 (2014).

[15] L. P. Regnault, J. Y. Henry, J. Rossat-Mignod, and A. De Combarieu, Magnetic properties of the layered nickel compounds $BaNi_2(PO_4)_2$ and $BaNi_2(AsO_4)_2$, J. Magn. Magn. Mater. **15-18**, 1021 (1980).

[16] G. Le Flem, R. Brec, G. Ouvard, A. Louisy, and P. Segransan, Magnetic interactions in the layer compounds MPX_3 (M = Mn, Fe, Ni; X = S, Se), J. Phys. Chem. Solids **43**, 455 (1982).

[17] J. H. Roudebush, N. H. Andersen, R. Ramlau, V. O. Garlea, R. Toft-Petersen, P. Norby, R. Schneider, J. N. Hay, and R. J. Cava, Structure and magnetic properties of $Cu_3Ni_2SbO_6$ and $Cu_3Co_2SbO_6$ delafossites with honeycomb lattices, Inorg. Chem. **52**, 6083 (2013).

[18] E. M. Seibel, J. H. Roudebush, H. Wu, Q. Huang, M. N. Ali, H. Ji, and R. J. Cava, Structure and magnetic properties of the $\alpha - NaFeO_2$-type honeycomb compound $Na_3Ni_2BiO_6$, Inorg. Chem. **52**, 13605 (2013).

[19] A. R. Wildes, V. Simonet, E. Ressouche, G. J. McIntyre, M. Avdeev, E. Suard, S. A. J. Kimber, D. Lançon, G. Pepe, B. Moubaraki, and T. J. Hicks, Magnetic structure of the quasi-two-dimensional antiferromagnet $NiPS_3$, Phys. Rev. B **92**, 224408 (2015).

[20] S. T. Bramwell, A. M. Buckley, and P. Day, The magnetic structure of $KNiAsO_4$: A two-dimensional honeycomb lattice, J. Solid State Chem. **111**, 48 (1994).

[21] N. Rogado, Q. Huang, J. W. Lynn, A. P. Ramirez, D. Huse, and R. J. Cava, $BaNi_2V_2O_8$: A two-dimensional honeycomb antiferromagnet, Phys. Rev. B **65**, 144443 (2002).

[22] B. Elbali, A. Boukhari, J. Aride, M. Belaiche, F. Abraham, and M. Drillon, Crystal structure and magnetic properties of $Ba_2Ni(PO_4)_2$, Eur. J. Solid State Inorg. Chem. **31**, 61 (1994).

[23] N. Faza, W. Treutmann, and D. Babel, Struktur- und magnetochemische Untersuchungen an den ternären Phosphaten $Ba_2M^{II}(PO_4)_2$ (M^{II} = Mn, Co) und Strukturverfeinerung von $BaNi_2(PO_4)_2$, Z. Anorg. Allg. Chem. **627**, 687 (2001).

[24] Z. He, W. Zhang, T. Xia, W. Yu, and W. Cheng, Crystal structure and magnetic properties of $Pb_2Ni(PO_4)_2$, Dalton Trans. **42**, 5480 (2013).

[25] FULLPROF suite, http://www.ill.eu/sites/fullprof/.

[26] K. Koepernik and H. Eschrig, Full-potential nonorthogonal local-orbital minimum-basis band-structure scheme, Phys. Rev. B **59**, 1743 (1999).

[27] J. P. Perdew and Y. Wang, Accurate and simple analytic representation of the electron-gas correlation energy, Phys. Rev. B **45**, 13244 (1992).

[28] E. A. Zvereva, M. I. Stratan, Y. A. Ovchenkov, V. B. Nalbandyan, J.-Y. Lin, E. L. Vavilova, M. F. Iakovleva, M. Abdel-Hafiez, A. V. Silhanek, X.-J. Chen, A. Stroppa, S. Picozzi, H. O. Jeschke, R. Valentí, and A. N. Vasiliev, Zigzag antiferromagnetic quantum ground state in monoclinic honeycomb lattice antimonates $A_3Ni_2SbO_6$ (A = Li, Na), Phys. Rev. B **92**, 144401 (2015).

[29] A.-M. Pradipto, R. Broer, and S. Picozzi, *Ab initio* modeling of magnetic anisotropy in Sr_3NiPtO_6, Phys. Chem. Chem. Phys. **18**, 4078 (2016).

[30] Z. He, S. C. Chen, C. S. Lue, W. Cheng, and Y. Ueda, Two magnetic orderings and a spin-flop transition in spin-1 system $SrNi_2(PO_4)_2$, Phys. Rev. B **78**, 212410 (2008).

[31] B. Koteswararao, R. Kumar, P. Khuntia, S. Bhowal, S. K. Panda, M. R. Rahman, A. V. Mahajan, I. Dasgupta, M. Baenitz, K. H. Kim, and F. C. Chou, Magnetic properties and heat capacity of the three-dimensional frustrated $S = 1/2$ antiferromagnet $PbCuTe_2O_6$, Phys. Rev. B **90**, 035141 (2014).

[32] A. Yogi, N. Ahmed, R. Nath, A. A. Tsirlin, S. Kundu, A. V. Mahajan, J. Sichelschmidt, B. Roy, and Y. Furukawa, Antiferromagnetism of $Zn_2VO(PO_4)_2$ and the dilution with Ti^{4+}, Phys. Rev. B **91**, 024413 (2015).

[33] R. J. Goetsch, V. K. Anand, A. Pandey, and D. C. Johnston, Structural, thermal, magnetic, and electronic transport properties of the $LaNi_2(Ge_{1-x}P_x)_2$ system, Phys. Rev. B **85**, 054517 (2012).

[34] H. Xiang, C. Lee, H.-J. Koo, X. Gong, and M.-H. Whangbo, Magnetic properties and energy-mapping analysis, Dalton Trans. **42**, 823 (2013).

[35] S. Maekawa, *Physics of Transition Metal Oxides* (Springer, Berlin, 2004), pp. 22–23.

[36] K. M. Ranjith, R. Nath, M. Majumder, D. Kasinathan, M. Skoulatos, L. Keller, Y. Skourski, M. Baenitz, and A. A. Tsirlin, Commensurate and incommensurate magnetic order in spin-1 chains stacked on the triangular lattice in $Li_2NiW_2O_8$, Phys. Rev. B **94**, 014415 (2016).

[37] B.N. Figgis, *Introduction to Ligand Fields* (Interscience, New York, 1966).

[38] P. H. Y. Li, R. F. Bishop, D. J. J. Farnell, and C. E. Campbell, Phase diagram of a frustrated Heisenberg antiferromagnet on the honeycomb lattice: The $J_1 - J_2 - J_3$ model, Phys. Rev. B **86**, 144404 (2012).

[39] T. Sakai and M. Takahashi, Effect of the Haldane gap on quasi-one-dimensional systems, Phys. Rev. B **42**, 4537 (1990).

[40] A. Zheludev, T. Masuda, I. Tsukada, Y. Uchiyama, K. Uchinokura, P. Böni, and S.-H. Lee, Magnetic excitations in coupled Haldane spin chains near the quantum critical point, Phys. Rev. B **62**, 8921 (2000).

[41] A. K. Bera, B. Lake, A. T. M. N. Islam, O. Janson, H. Rosner, A. Schneidewind, J. T. Park, E. Wheeler, and S. Zander, Consequences of critical interchain couplings and anisotropy on a Haldane chain, Phys. Rev. B **91**, 144414 (2015).

[42] R. M. Morra, W. J. L. Buyers, R. L. Armstrong, and K. Hirakawa, Spin dynamics and the Haldane gap in the spin-1 quasi-one-dimensional antiferromagnet $CsNiCl_3$, Phys. Rev. B **38**, 543 (1988).

[43] K. Momma and F. Izumi, *VESTA* 3 for three-dimensional visualization of crystal, volumetric and morphology data, J. Appl. Crystallogr. **44**, 1272 (2011).